Forced rotation enhances cylinder flow-induced vibrations at subcritical Reynolds number

Rémi Bourguet†

Institut de Mécanique des Fluides de Toulouse, Université de Toulouse and CNRS, Toulouse 31400, France

When a cylinder is mounted on an elastic support within a current, vortex-induced vibrations (VIV) may occur down to a Reynolds number (Re) close to 20, based on the body diameter (D) and inflow velocity (U), i.e. below the critical value of 47 reported for the onset of flow unsteadiness when the body is fixed. The impact of a forced rotation of the elastically mounted cylinder on the system behaviour is explored numerically for $Re \leqslant 30$, over wide ranges of values of the rotation rate (ratio between body surface velocity and U, $\alpha \in [0, 5]$) and reduced velocity (inverse of the oscillator natural frequency non-dimensionalized by D and U, $U^\star \in [2, 30]$). The influence of the rotation is not monotonic, but the most prominent effect uncovered in this work is a substantial enhancement of the subcritical-Re, flow-induced vibrations beyond $\alpha = 2$. This enhancement is twofold. First, the rotation results in a considerable expansion of the vibration/flow unsteadiness region in the (Re, $U^\star$) domain, down to $Re = 4$. Second, the elliptical orbits described by the rotating body are subjected to a major amplification, with a transition from VIV to responses whose magnitude tends to increase unboundedly with $U^\star$, even though still synchronized with flow unsteadiness. The emergence of such galloping-like oscillations close to the onset of vibrations disrupts the scenario of gradual vibration growth with Re, as amplitudes larger than 10 body diameters may be observed at $Re = 10$.

Key words: flow–structure interactions, vortex streets, wakes

1. Introduction

The flow past a fixed circular cylinder becomes unsteady beyond a critical Reynolds number close to 47, with the formation of the alternating von Kármán vortices (Mathis, Provansal & Boyer [1984](#)). The Reynolds number (Re) is based on the body diameter
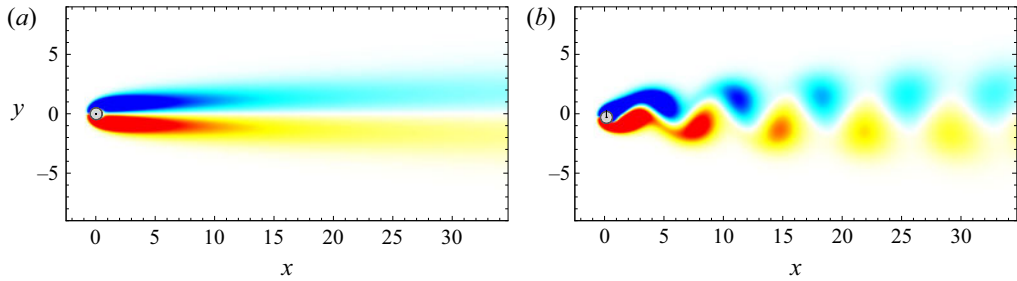
† Email address for correspondence: remi.bourguet@imft.fr

Figure 1. Flow past a non-rotating, elastically mounted cylinder at $Re = 25$: instantaneous isocontours of spanwise vorticity ($\omega_z \in [-0.4, 0.4]$) for (*a*) $U^\star = 4$ (no vibration) and (*b*) $U^\star = 8$ (cross-flow vibration amplitude equal to $0.31D$). Positive/negative vorticity values are plotted in red/blue. The trajectory of the cylinder centre is indicated by a black line. Part of the computational domain is shown.

(D) and inflow velocity (U). The above critical value is denoted by Re_c^f in the following with reference to the fixed body. When the cylinder is mounted on an elastic support, vortex-induced vibrations (VIV), and thus flow unsteadiness, may occur in the subcritical-Re range, i.e. for $Re < Re_c^f$, possibly down to $Re \approx 20$, depending on the system parameters (Cossu & Morino 2000; Mittal & Singh 2005; Kou *et al.* 2017; Dolci & Carmo 2019; Boersma *et al.* 2021).

Among the different forms of flow-induced vibrations (FIV), VIV represent a paradigm of fluid–structure interaction involving synchronization, or lock-in, between body motion and flow unsteadiness. Owing to their impact on engineering structures, they have been the object of a number of studies at higher Re, as reviewed, for example, by Williamson & Govardhan (2004). Regardless of the Re value, VIV develop over a well-delimited range of the reduced velocity, $U^\star$, defined as the inverse of the oscillator natural frequency non-dimensionalized by D and U. Within this range, where lock-in is established, VIV amplitudes exhibit bell-shaped trends as functions of $U^\star$ and are generally of the order of D in the cross-flow direction, and one or more orders of magnitude lower in the streamwise direction. A typical case of VIV at subcritical Re is visualized in figure 1. The flow, which is steady in the absence of vibration (figure 1*a*), becomes unsteady and synchronizes with cylinder oscillation once VIV appear (figure 1*b*).

The present work explores the impact of a forced rotation of the elastically mounted cylinder at subcritical Re. The rotation breaks the symmetry of the system and may result in a profound alteration of its behaviour, as illustrated in prior studies for $Re > Re_c^f$ (Stansby & Rainey 2001; Yogeswaran & Mittal 2011; Bourguet & Lo Jacono 2014; Zhao, Cheng & Lu 2014; Seyed-Aghazadeh & Modarres-Sadeghi 2015; Wong *et al.* 2017; Bourguet 2020*a*; Munir *et al.* 2021). In particular, the rotation distorts the bell-shaped trends of VIV amplitudes versus $U^\star$, as well as body trajectories, i.e. from figure-of-eight to elliptical orbits. It can also trigger responses that resemble the galloping oscillations usually reported for non-axisymmetric bodies, with amplitudes increasing unlimitedly with $U^\star$. Such responses are accompanied by a reconfiguration of the flow and a myriad of multi-vortex wake patterns. These aspects remain to be examined at subcritical Re. In addition, the boundaries of the vibration region in the ($Re, U^\star$) domain are expected to be reshaped by the rotation and need to be determined; this includes the question of the evolution of the lowest value of Re for the onset of flow unsteadiness. An attempt is proposed here on the basis of numerical simulations.
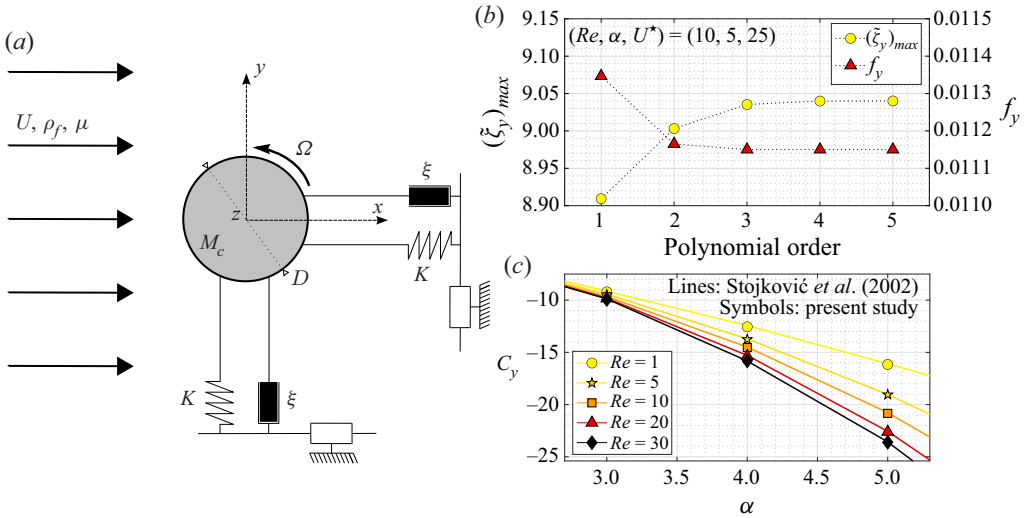
955 R3-2

Figure 2. (*a*) Sketch of the physical system. (*b*) CF vibration amplitude and frequency as functions of the polynomial order for $(Re, \alpha, U^\star) = (10, 5, 25)$. (*c*) CF force coefficient as a function of α for a rigidly mounted cylinder, over a range of *Re*; the present results are compared to those reported by Stojković *et al.* (2002).

The subcritical-*Re* behaviour of the flow–structure system is investigated over a wide range of values of the rotation rate, defined as the ratio between cylinder surface and inflow velocities, $\alpha \in [0, 5]$, for reduced velocities up to $U^\star = 30$. This parameter space encompasses the appearance of the above-mentioned galloping-like responses at higher *Re*. Focus is placed on $Re \leqslant 30$, for which the flow past a rigidly mounted cylinder remains steady over the selected α range (Stojković, Breuer & Durst 2002).

2. Formulation and numerical method

A sketch of the physical system is presented in figure 2(*a*). The elastically mounted circular cylinder of diameter D and mass per unit length M_c is parallel to the z axis and placed in an incompressible uniform cross-current of velocity U, density ρ_f and viscosity μ aligned with the x axis. The Reynolds number, $Re = \rho_f U D / \mu$, is kept below or equal to 30. The flow is two-dimensional across the parameter space investigated. This point has been verified via three-dimensional simulations initialized with three-dimensional flow fields. The two-dimensional Navier–Stokes equations are employed to predict the flow dynamics. The cylinder is free to translate in the in-line (IL, x axis) and cross-flow (CF, y axis) directions. The structural stiffnesses (K) and damping ratios (ξ) of the elastic support are the same in both directions. All the physical variables are non-dimensionalized by D, U and ρ_f. The IL and CF displacements, non-dimensionalized by D, are denoted by ζ_x and ζ_y. The IL and CF force coefficients are defined as $C_{\{x,y\}} = 2F_{\{x,y\}}/(\rho_f D U^2)$, where F_x and F_y are the dimensional fluid forces per unit length, aligned with the x and y axes. The dynamics of the two-degree-of-freedom oscillator is governed by the following equations:

$$\ddot{\zeta}_{\{x,y\}} + \frac{4\pi\xi}{U^\star}\dot{\zeta}_{\{x,y\}} + \left(\frac{2\pi}{U^\star}\right)^2 \zeta_{\{x,y\}} = \frac{C_{\{x,y\}}}{2m}, \tag{2.1}$$

where the dot $\dot{}$ designates the non-dimensional time derivative. The non-dimensional mass of the structure is defined as $m = M_c/(\rho_f D^2)$. The ratio between the mass of the

structure and the mass of the displaced fluid is equal to $4\,m/\pi$. The reduced velocity is defined as $U^{\star} = 1/f_n$, where $f_n = [D/(2\pi U)]\sqrt{K/M_c}$ is the non-dimensional natural frequency in vacuum. The cylinder is subjected to a forced, anticlockwise, steady rotation about its axis. The rotation is controlled by the rotation rate $\alpha = \Omega D/(2U)$, where Ω is the angular velocity of the cylinder. The values of m and ξ are set to 10 and 0, while $U^{\star}$ is varied from 2 to 30 and α ranges from 0 to 5.

The numerical method is the same as in previous studies concerning comparable systems at higher *Re* (Bourguet & Lo Jacono 2014; Bourguet 2020*a*). It is briefly summarized here and some additional convergence/validation results are presented. The coupled flow–structure equations are solved by the parallelized code *Nektar*, which is based on the spectral/*hp* element method (Karniadakis & Sherwin 1999). A large rectangular computational domain is considered (350*D* downstream and 250*D* in front, above and below the cylinder) to avoid any spurious blockage effects due to domain size. It is discretized into 3975 spectral elements. A no-slip condition is applied on the cylinder surface.

A convergence study in a typical case of subcritical-*Re* vibrations at the highest rotation rate, $(Re, \alpha, U^{\star}) = (10, 5, 25)$, is presented in figure 2(*b*). The evolutions of the CF vibration amplitude (where the tilde ˜ designates the fluctuation about the time-averaged value) and frequency (f_y) as functions of the spectral element polynomial order show that an increase from order four to order five has no impact on the results. The convergence study was repeated up to $Re = 30$ and a polynomial order equal to four was selected. A comparable procedure was employed to set the non-dimensional time step to 0.005. In figure 2(*c*), a comparison of C_y values over ranges of α and *Re* for a rigidly mounted cylinder, with the results reported by Stojković *et al.* (2002), confirms the validity of the present numerical method.

Each simulation is initialized with the established flow past a fixed body at the selected *Re*. Then the rotation is started and the body is released. The analysis is based on time series collected after convergence, over 30 oscillation cycles in the unsteady cases.

3. Flow–structure system behaviour at subcritical Reynolds number

The boundaries of the vibration/unsteady flow region are examined in § 3.1. Vibration amplitudes and frequencies, as well as body trajectories, are presented in § 3.2. Flow physics and synchronization with body motion are addressed in § 3.3. Some salient properties of fluid forces are reported in § 3.4.

3.1. *Vibration/unsteady flow region*

The evolution of the vibration region as α is increased from 0 to 5 is depicted in figure 3(*a*–*h*). The coloured areas delimit the regions of the (*Re*, $U^{\star}$) domain where the body oscillates and the flow is unsteady; outside of these regions the flow–structure system is steady. The impact of the rotation is not monotonic, as the vibration region first tends to shrink, up to $\alpha = 1$, and then expands. For $\alpha = 5$, it covers most of the parameter space investigated.

The lowest value of *Re* where vibrations arise (Re_c) and the corresponding value of $U^{\star}$ ($U^{\star}_c$) are plotted as functions of α in figure 3(*i*, *j*); Re_c is the critical *Re* in the elastically mounted body case. It is recalled that the term 'subcritical' employed in this paper refers to the critical *Re* for flow unsteadiness in the fixed body case ($Re_c^f = 47$). From a value close to 20 in the absence of rotation, also reported in prior works (e.g. Mittal & Singh 2005),
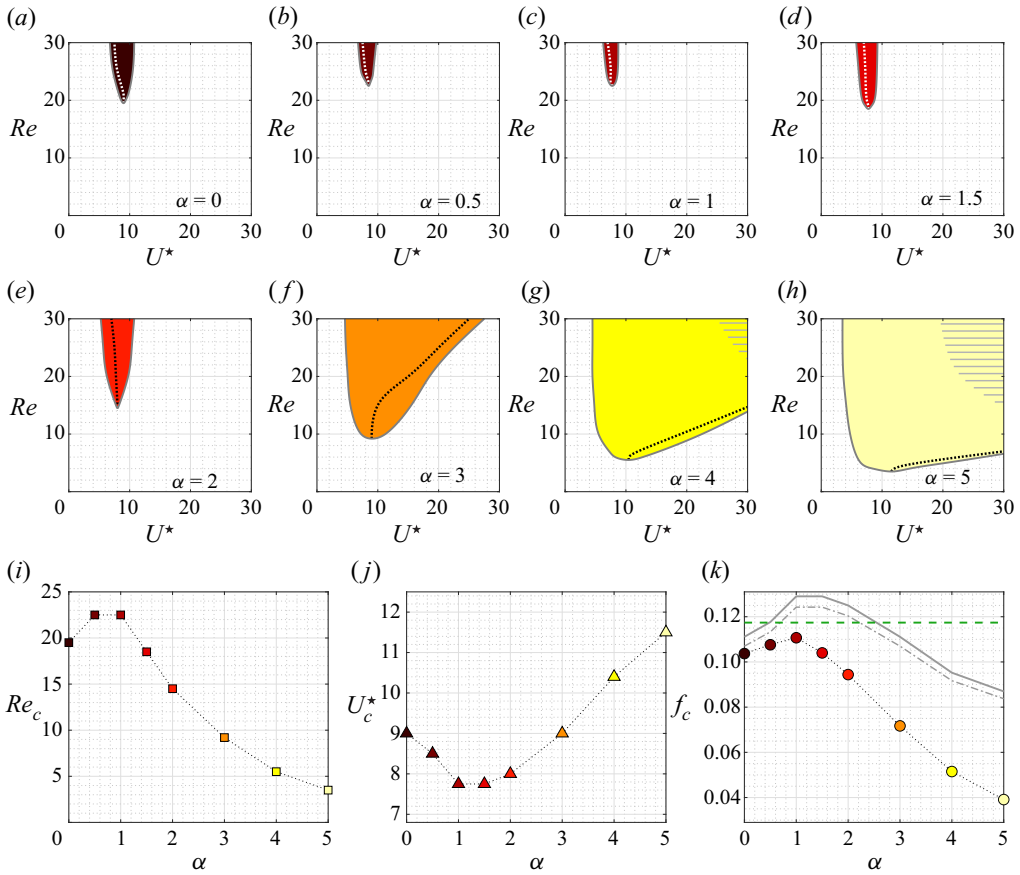
Figure 3. (*a–h*) Vibration/unsteady flow region as a function of Re and $U^\star$, for $\alpha \in [0, 5]$; the α value is specified in each panel, a dotted line indicates the value of $U^\star$ where the peak amplitude is reached, and horizontal stripes denote the vortex fragmentation region in panels (*g*) and (*h*). (*i*) Lowest value of the Reynolds number where vibrations/flow unsteadiness occur, and corresponding values of the (*j*) reduced velocity and (*k*) CF vibration frequency, as functions of α. The colour code associated with α ranges from dark brown ($\alpha = 0$) to light yellow ($\alpha = 5$). In panel (*k*), the natural frequency in vacuum and the corrected natural frequency, with an added-mass coefficient of 1, are indicated by full and dash-dotted grey lines, respectively; the green dashed line represents the critical frequency of flow unsteadiness in the fixed cylinder case (Cossu & Morino 2000).

Re_c is found to increase slightly for low α and then decrease down to approximately 4 for $\alpha = 5$. As shown in figure 3(*k*), the CF oscillation frequency at the onset of vibrations (f_c), which coincides with the flow unsteadiness frequency as discussed in § 3.3, globally follows the trend of the natural frequency in vacuum ($1/U_c^\star$, grey full line) but remains lower. It also departs from the natural frequency modified by considering the potential added-mass coefficient $C_m = 1$ (i.e. $\sqrt{m/(m + C_m\pi/4)}/U_c^\star$, grey dash-dotted line). The frequency may substantially deviate from that observed in the wake of a fixed cylinder at Re_c^f (green dashed line; Cossu & Morino 2000).

3.2. *Vibration properties*

The vibration amplitudes are examined in figure 4(*a–h*), which represents the maximum fluctuation of the CF displacement about its time-averaged value, as a function of $U^\star$
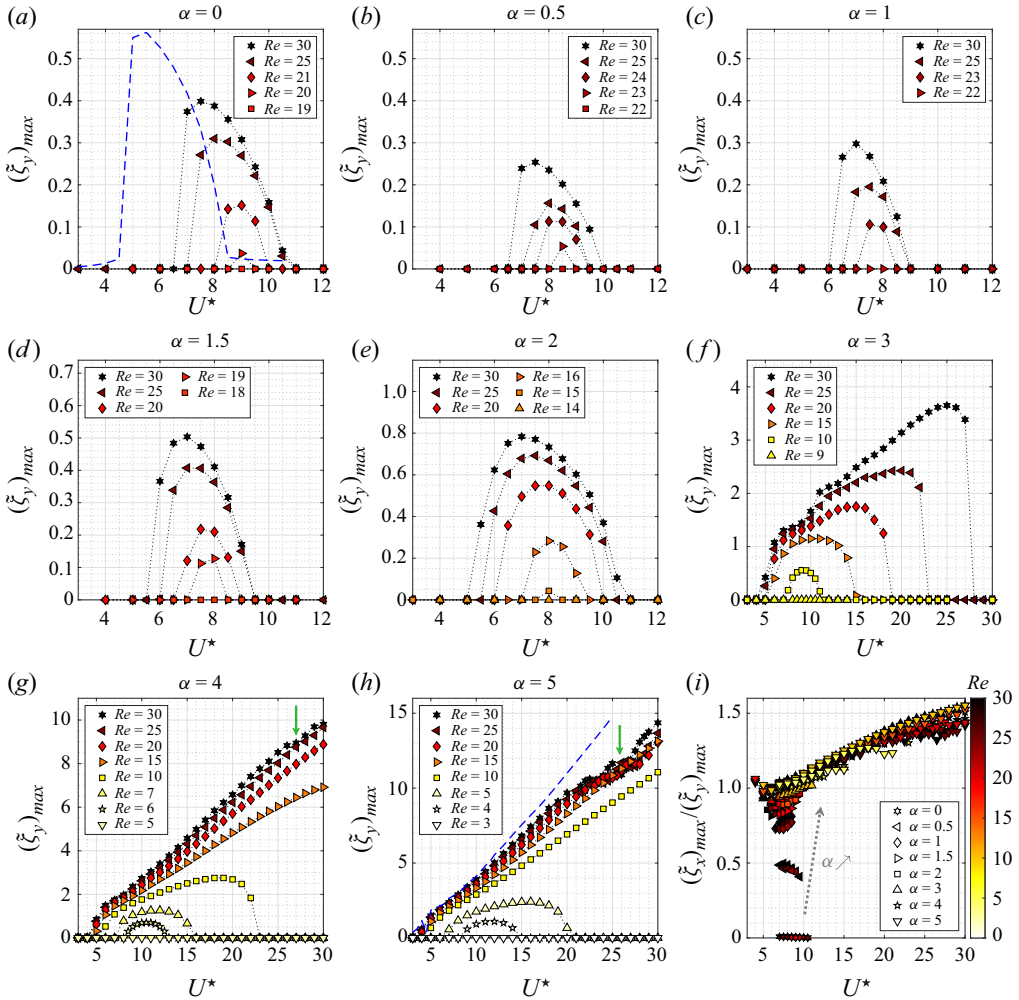
Figure 4. (*a–h*) CF vibration amplitude as a function of $U^\star$, over a range of Re, for $\alpha \in [0, 5]$; the α value is specified in each panel. The amplitudes previously reported at $Re = 100$ (Bourguet 2020*a*) are represented by blue dashed lines in panels (*a*) and (*h*). In panels (*g*) and (*h*), green arrows indicate the irregular evolutions associated with vortex fragmentation. (*i*) Ratio of IL and CF vibration amplitudes as a function of $U^\star$, for all studied cases where vibrations develop; the α value is indicated by symbol shape and the Re value by its colour. The grey dotted arrow denotes the trend observed when α is increased.

over a range of Re. Each panel corresponds to a given rotation rate, $\alpha \in [0, 5]$. For the non-rotating body, the gradual amplification of the bell-shaped curve, typical of VIV, as Re is increased, is accompanied by a shift of the peak amplitude towards lower $U^\star$ values. This is the onset of a trend that persists beyond the subcritical-Re range, as illustrated by the results reported at $Re = 100$ in a prior work (blue dashed line; Bourguet 2020*a*). The rotation modulates the width and magnitude of the amplitude bell-shaped curve, but its regular evolution with Re remains comparable for each α, up to $\alpha = 2$. In particular, the shift of the peak amplitude towards lower $U^\star$ values can be visualized in figure 3(*a–e*) (dotted lines). The influence of the rotation is more pronounced for higher α: the $U^\star$ values associated with the peak amplitude and upper boundary of the vibration region are found to increase rapidly with Re, and exceed the limit of the parameter space under study, as
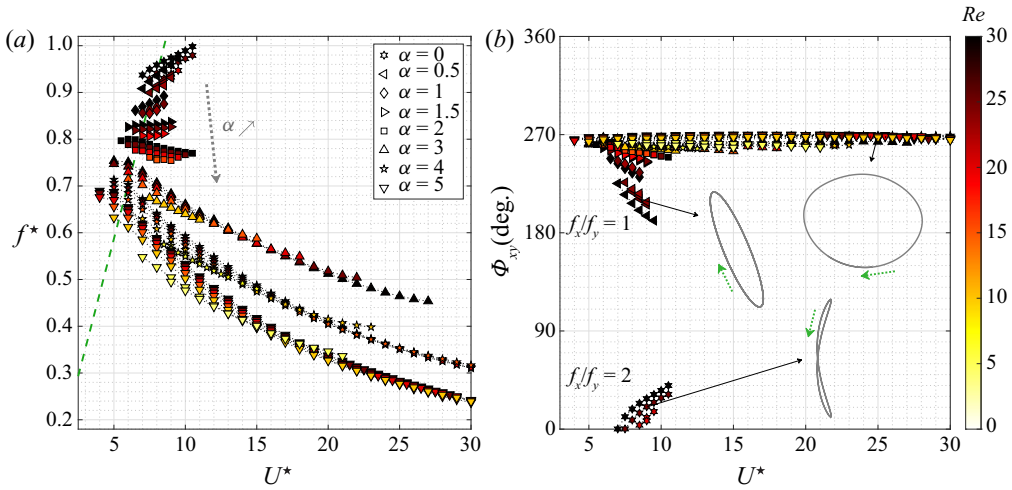
955 R3-6

Figure 5. (*a*) CF vibration frequency normalized by f_n and (*b*) IL/CF vibration phase difference as functions of $U^\star$, over a range of Re, for $\alpha \in [0, 5]$; the α value is indicated by symbol shape and the Re value by its colour. In panel (*a*), the green dashed line denotes the critical frequency of flow unsteadiness in the fixed cylinder case (Cossu & Morino 2000), normalized by f_n, and the grey dotted arrow represents the trend observed when α is increased. In panel (*b*), the IL/CF vibration frequency ratio is specified and three typical trajectories are depicted (not at scale); green dotted arrows indicate the direction of motion.

also depicted in figure 3(*f–h*). Such behaviour was previously identified at supercritical *Re* and the responses were named galloping-like, in reference to the seemingly unbounded growth of their amplitudes with $U^\star$; a typical case is plotted in figure 4(*h*) ($Re = 100$, blue dashed line). The present results show that these large-amplitude oscillations may arise in the subcritical-*Re* range, close to the onset of vibrations, e.g. amplitudes larger than 10*D* are observed at $Re = 10$ for $\alpha = 5$. Additional simulations indicate that this phenomenon persists when a low level of structural damping is introduced (up to $\xi = 5\%$) and *m* is varied between 5 and 20.

The ratio between the IL and CF vibration amplitudes is considerably impacted by the rotation, as shown in figure 4(*i*), where this ratio is plotted for all vibrating body cases as a function of $U^\star$. Compared to the influence of α, the effect of *Re* is found to remain marginal within the subcritical range examined here. In the absence of rotation, the IL responses are very small compared to the CF ones, as also noted in prior studies concerning subcritical-*Re* VIV (Mittal & Singh 2005). As indicated by the grey dotted arrow in figure 4(*i*), the amplitude ratio increases sharply with α and it reaches approximately 1.5 in the high-$U^\star$ range.

The vibrations are periodic and dominated by a single frequency in each direction, f_x and f_y. The CF vibration frequency normalized by the natural frequency in vacuum, $f^\star = f_y/f_n$, is plotted as a function of $U^\star$ in figure 5(*a*). Three elements can be noted. First, the vibration frequency remains lower than f_n. Second, $f^\star$ globally decreases as α is increased (grey dotted arrow); it reaches very low values for high α, especially compared to the critical frequency in the wake of a fixed cylinder (green dashed line). Third, the evolution of $f^\star$ with $U^\star$ at a given α progressively shifts from increasing trends in the low-α range to decreasing trends for higher α. The present subcritical-*Re* vibrations generally exhibit lower frequencies than the responses encountered at higher *Re*. However, the proximity of the above properties (second and third points) with those reported at $Re = 100$

955 R3-7

(Bourguet 2020*a*) emphasizes the continuity of the system behaviour between the subcritical- and supercritical-*Re* ranges.

The rotation breaks the CF symmetry of the system, which induces a switch of f_x/f_y from 2 to 1, and a transition from figure-of-eight trajectories of the body to elliptical orbits. The shape and orientation of the trajectory is determined by the phase difference, $\Phi_{xy} = \phi_x - n\phi_y$, where ϕ_x and ϕ_y are the IL and CF response phases ($n = 1$ except for $\alpha = 0$, where $n = 2$). The evolution of Φ_{xy} is represented in figure 5(*b*), along with typical trajectories. For $\alpha = 0$, Φ_{xy} varies between $0°$ and $45°$: the figure-of-eight trajectories are close to a crescent bent downstream and the body moves upstream when reaching CF oscillation maxima. Similar orbits were noted for subcritical-*Re* VIV of flexible cylinders (Bourguet 2020*b*). Once the body rotates, Φ_{xy} ranges from $180°$ to $270°$, and converges close to the latter value for high α: the cylinder describes clockwise elliptical orbits, i.e. counter-rotating relative to the forced rotation.

3.3. *Flow–body synchronization and wake patterns*

The emergence of large-amplitude, galloping-like vibrations (e.g. figure 4*h*) raises the question of the synchronization with the flow, since galloping oscillations do not usually involve such a lock-in condition. It appears that the frequency of flow unsteadiness (determined from time series of the CF component of flow velocity in the wake) always coincides with the vibration frequency (f_y). Flow–body synchronization is thus established in all cases. The persistence of lock-in and the fact that a quasi-steady approach, similar to that described in Bourguet (2020*a*), fails to predict the responses suggests that the interaction with flow unsteadiness plays a role in sustaining body motion, even if the vibrations resemble galloping oscillations.

In contrast with the fragmented multi-vortex patterns reported at higher *Re* (e.g. Munir *et al.* 2021), the present wakes are composed of a pair of counter-rotating vortices formed per oscillation cycle over most of the vibration regions, including for large response amplitudes (figure 6*a–c*). The antisymmetric organization observed for $\alpha = 0$ (figure 1*b*) is significantly distorted and the vortical structures may reach very large scales. Vortex fragmentation occurs close to the upper edge of the $(Re, U^\star)$ domain for high α (horizontally striped areas in figure 3*g,h*), as illustrated in figure 6(*d*). The transition between fragmented patterns, typically the addition/subtraction of one vortex per cycle as $U^\star$ is varied, is associated with irregular evolutions of vibration amplitudes (green arrows in figure 4*g,h*).

3.4. *Fluid forces*

The vibrations are accompanied by the appearance of fluctuations of fluid forces and by a modulation of their time-averaged values (denoted by a bar ⁻). For example, $\bar{C}_x$, which is slightly negative in the absence of vibration for $\alpha = 5$ at $Re = 15$, is amplified up to 3.4. Special attention is paid to the alteration of the Magnus effect, i.e. the CF force induced by the rotation. No major modification of $\bar{C}_y$ is observed for low α. For each $\alpha > 1$, $\bar{C}_y$ is found to increase consistently with the time-averaged magnitude of the relative flow velocity seen by the moving body, defined as $V = \{1 - \dot{\zeta}_x, -\dot{\zeta}_y\}^T$. This trend can be visualized in figure 7(*a*). The values of C_y for a rigidly mounted cylinder are indicated by green areas. As shown in figure 7(*b*), a normalization of α by the time-averaged magnitude of the relative velocity tends to collapse $\bar{C}_y$ values close to those measured in the absence of vibration (green area; the grey dashed line denotes the potential flow value, $C_y = -2\pi\alpha$, for comparison). A reasonable estimate of $\bar{C}_y$ can thus be obtained
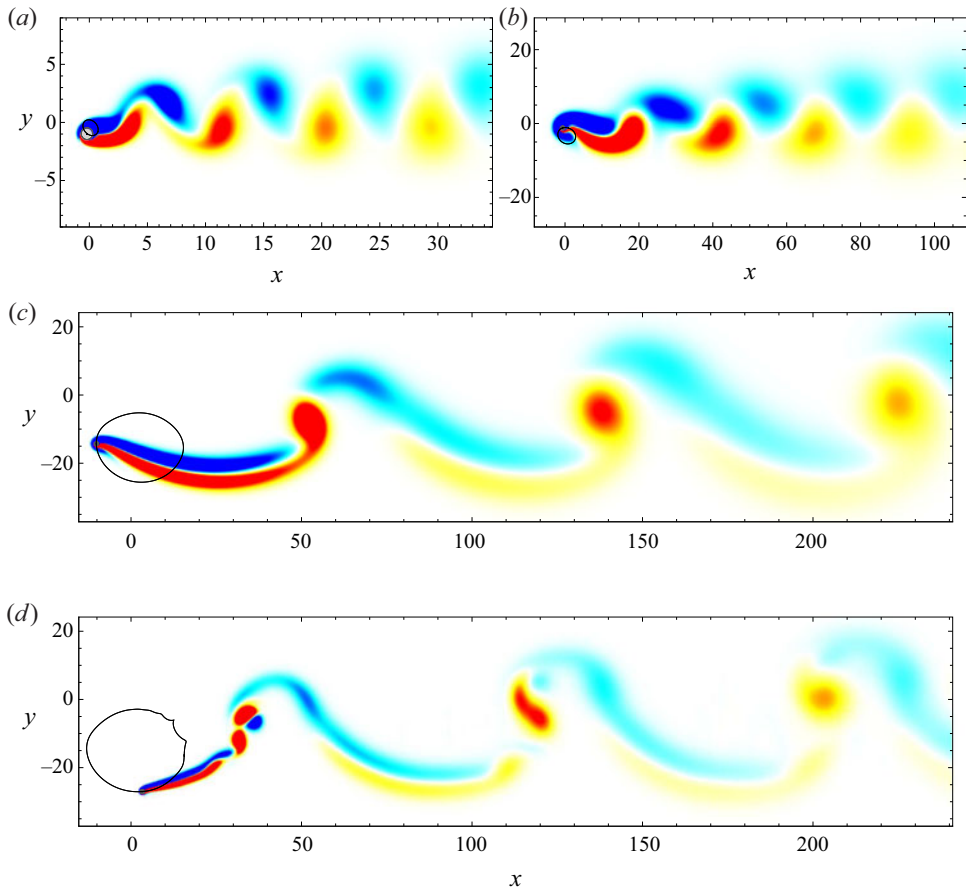
Figure 6. Instantaneous isocontours of spanwise vorticity for (*a*) $(Re, \alpha, U^\star) = (25, 2, 8)$ ($\omega_z \in [-0.3, 0.3]$), (*b*) $(Re, \alpha, U^\star) = (5, 5, 12)$ ($\omega_z \in [-0.03, 0.03]$), (*c*) $(Re, \alpha, U^\star) = (10, 5, 25)$ ($\omega_z \in [-0.03, 0.03]$) and (*d*) $(Re, \alpha, U^\star) = (25, 5, 25)$ ($\omega_z \in [-0.05, 0.05]$). Positive/negative vorticity values are plotted in red/blue. The trajectory of the cylinder centre is indicated by a black line. Part of the computational domain is shown.

based on the only knowledge of body dynamics. The above collapse does not persist at higher *Re* (e.g. *Re* = 100); some deviations can already be noted at *Re* ⩾ 25. It appears to be a specific property of the low, subcritical-*Re* range.

Another typical property relates to force–displacement phasing. For periodic vibrations without structural damping, the system may exhibit two possible states where the force is either in phase with the displacement, when $f_{\{x,y\}} < f_n$, or in phase opposition, when $f_{\{x,y\}} > f_n$. While both phasing states are usually encountered at higher *Re* once the body rotates (i.e. $f_x = f_y$; Bourguet 2020*a*), here, only the former state is observed.

4. Conclusions

The subcritical-*Re* FIV of a cylinder subjected to a forced rotation have been investigated numerically for *Re* ⩽ 30, over wide ranges of α and $U^\star$ values. Compared to the non-rotating body case, the region of the $(Re, U^\star)$ domain where vibrations and flow unsteadiness occur shrinks for low rotation rates and then expands for higher α. From a
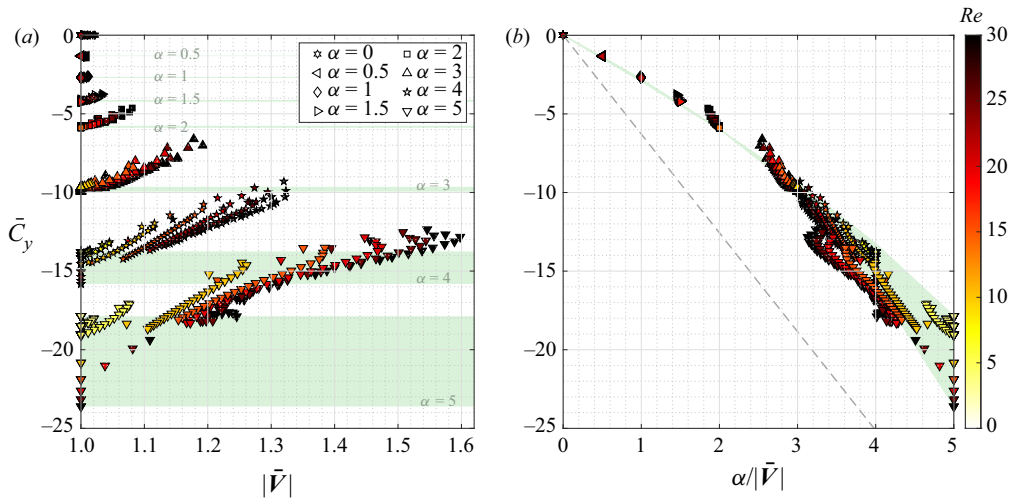
Figure 7. Time-averaged CF force coefficient as a function of (*a*) the time-averaged magnitude of the relative flow velocity seen by the body and (*b*) α normalized by the time-averaged magnitude of the relative flow velocity, over a range of *Re*, for $\alpha \in [0, 5]$; the α value is indicated by symbol shape and the *Re* value by its colour. The green areas encompass C_y values for a rigidly mounted body, over the range of *Re* investigated. In panel (*b*), the grey dashed line represents the potential flow value ($C_y = -2\pi\alpha$).

value close to 20 in the absence of rotation, the *Re* associated with the onset of vibrations is found to decrease down to approximately 4 for $\alpha = 5$.

Under forced rotation, the vibration amplitudes are comparable in both directions, and even larger in the IL direction than in the CF direction for high $U^\star$, which contrasts with the non-rotating body case. The typical trajectory of the rotating cylinder is an elliptical orbit, oriented in the opposite direction relative to the forced rotation, with a frequency lower than f_n. Up to $\alpha = 2$, the bell-shaped curves of vibration amplitudes versus $U^\star$, typical of VIV, are modulated by the rotation but their regular growth with *Re* remains analogous to that reported for $\alpha = 0$. The impact of the rotation on the scenario of vibration growth with *Re* is more pronounced for $\alpha > 2$: while the upper $U^\star$ boundary of the vibration region rapidly increases with *Re*, vibration amplitudes seem to grow unboundedly with $U^\star$ and their frequencies reach very low values. These galloping-like responses, previously identified at higher *Re*, thus arise in the subcritical-*Re* range, close to the onset of vibrations. For example, amplitudes larger than 10 diameters are encountered at $Re = 10$ for $\alpha = 5$.

Body motion and flow unsteadiness are synchronized in all cases, regardless of vibration amplitudes. Except close to the upper edge of the (Re, $U^\star$) domain, where vortices tend to fragment, the wake is composed of a pair of counter-rotating and possibly very large vortices per oscillation cycle. The occurrence of FIV is accompanied by the appearance of fluid force fluctuations and by a modification of their time-averaged values. In particular, the alteration of the Magnus effect at subcritical *Re* is found to be closely connected to the relative flow velocity seen by the vibrating body.

To summarize, the influence of the rotation on the flow–structure system behaviour is not monotonic, but the most prominent effect uncovered here is a substantial enhancement of subcritical-*Re* FIV for high α. This enhancement is twofold: a considerable expansion of the vibration region, down to very low *Re*, and a major amplification of the structural responses, with the emergence of galloping-like oscillations.

955 R3-10

Author ORCIDs.
 Rémi Bourguet https://orcid.org/0000-0001-8079-3140.

REFERENCES

BOERSMA, P.R., ZHAO, J., ROTHSTEIN, J.P. & MODARRES-SADEGHI, Y. 2021 Experimental evidence of vortex-induced vibrations at subcritical Reynolds numbers. *J. Fluid Mech.* **922**, R3.

BOURGUET, R. 2020*a* Two-degree-of-freedom flow-induced vibrations of a rotating cylinder. *J. Fluid Mech.* **897**, A31.

BOURGUET, R. 2020*b* Vortex-induced vibrations of a flexible cylinder at subcritical Reynolds number. *J. Fluid Mech.* **902**, R3.

BOURGUET, R. & LO JACONO, D. 2014 Flow-induced vibrations of a rotating cylinder. *J. Fluid Mech.* **740**, 342–380.

COSSU, C. & MORINO, L. 2000 On the instability of a spring-mounted circular cylinder in a viscous flow at low Reynolds numbers. *J. Fluids Struct.* **14**, 183–196.

DOLCI, D.I. & CARMO, B.S. 2019 Bifurcation analysis of the primary instability in the flow around a flexibly mounted circular cylinder. *J. Fluid Mech.* **880**, 1–11.

KARNIADAKIS, G.E. & SHERWIN, S. 1999 *Spectral/hp Element Methods for CFD*, 1st edn. Oxford University Press.

KOU, J., ZHANG, W., LIU, Y. & LI, X. 2017 The lowest Reynolds number of vortex-induced vibrations. *Phys. Fluids* **29**, 041701.

MATHIS, C., PROVANSAL, M. & BOYER, L. 1984 The Bénard–von Kármán instability: an experimental study near the threshold. *J. Phys. Lett.* **45**, 483–491.

MITTAL, S. & SINGH, S. 2005 Vortex-induced vibrations at subcritical *Re*. *J. Fluid Mech.* **534**, 185–194.

MUNIR, A., ZHAO, M., WU, H. & TONG, F. 2021 Flow-induced vibration of a rotating circular cylinder at high reduced velocities and high rotation rates. *Ocean Engng* **238**, 109562.

SEYED-AGHAZADEH, B. & MODARRES-SADEGHI, Y. 2015 An experimental investigation of vortex-induced vibration of a rotating circular cylinder in the crossflow direction. *Phys. Fluids* **27**, 067101.

STANSBY, P.K. & RAINEY, R.C.T. 2001 On the orbital response of a rotating cylinder in a current. *J. Fluid Mech.* **439**, 87–108.

STOJKOVIĆ, D., BREUER, M. & DURST, F. 2002 Effect of high rotation rates on the laminar flow around a circular cylinder. *Phys. Fluids* **14**, 3160.

WILLIAMSON, C.H.K. & GOVARDHAN, R. 2004 Vortex-induced vibrations. *Annu. Rev. Fluid Mech.* **36**, 413–455.

WONG, K.W.L., ZHAO, J., LO JACONO, D., THOMPSON, M.C. & SHERIDAN, J. 2017 Experimental investigation of flow-induced vibration of a rotating circular cylinder. *J. Fluid Mech.* **829**, 486–511.

YOGESWARAN, V. & MITTAL, S. 2011 Vortex-induced and galloping response of a rotating circular cylinder. In *IUTAM Symposium on Bluff Body Flows, IIT-Kanpur, India* (ed. S. Mittal & G. Biswas), pp. 153–156.

ZHAO, M., CHENG, L. & LU, L. 2014 Vortex induced vibrations of a rotating circular cylinder at low Reynolds number. *Phys. Fluids* **26**, 073602.